RSC Advances

PAPER

View Article Online
View Journal | View Issue

Cite this: *RSC Adv.*, 2025, **15**, 37348

Metal–organic framework-immobilized track-etched membrane with PVC nanofiber mats for carbon dioxide capture

Aigerim Kh. Shakayeva,[ab] Dias D. Omertassov,[ab] Zhanna K. Zhatkanbayeva,[b] Rafael I. Shakirzyanov,[b] Ainash T. Zhumazhanova,[ab] Olgun Güven[c] and Ilya V. Korolkov*[ab]

The increasing concentration of carbon dioxide in the atmosphere is a major cause of climate change, necessitating the development of efficient adsorbents for CO_2 capture. Traditional methods, such as adsorption using amines and cryogenic separation, are constrained by high energy consumption, equipment corrosion, and solvent degradation. Membrane technology can help overcome some of the problems associated with these traditional methods. Track-etched membranes (TeMs), with their unique properties, have been used as substrates for the preparation of composite membranes to capture CO_2. In this study, we synthesized HKUST-1 metal–organic frameworks (MOFs) by the solvothermal method and incorporated them into PVC nanofibers by electrospinning. The nanofibers were then deposited on PET TeMs. The secondary decoration of HKUST-1 was performed to increase the MOF concentration. The integration of MOFs improved adsorption capacity due to their high surface area and porosity. The obtained membranes were characterised by FTIR, XRD, SEM-EDX, BET, TGA, and contact angle measurements. The composite membrane exhibited a BET surface area of 135.26 $m^2\ g^{-1}$. The contact angle of the membrane was 95° ± 9°, indicating a hydrophobic nature. The PVC/HKUST-1(SD)@PET TeM was shown to have a CO_2 adsorption capacity of 1.48 mmol g^{-1} at 25 °C, with efficient regeneration properties. The CO_2 capturing capacity retains 94% of the initial value after 12 adsorption–desorption cycles. These results demonstrate the potential of the obtained membrane as an efficient, regenerable and adsorptive membrane for CO_2 capture.

Received 3rd July 2025
Accepted 23rd September 2025

DOI: 10.1039/d5ra04733a

rsc.li/rsc-advances

1. Introduction

The world is experiencing increasingly visible effects of climate change, including retreating glaciers and ice caps, more extreme weather, prolonged droughts, intensified tropical cyclones, and frequent wildfires due to excessive amounts of CO_2 in the atmosphere.[1,2] Anthropogenic activities are mainly responsible for the uncontrolled increase in atmospheric carbon dioxide levels, which has led to global temperature rises. Therefore, it has become crucial to implement immediate measures to curtail global greenhouse gas emissions to effectively mitigate the escalating effects of climate change.[3] Consequently, the development of effective technologies and new materials for carbon capture and storage (CCS) has become critical to achieving global climate goals.

The potential of various porous adsorbents for CO_2 adsorption has been the subject of numerous investigations. These include activated carbons,[4] zeolites,[5] silica materials,[6] metal–organic frameworks (MOFs),[7] and other porous materials.[8] The use of MOFs for CO_2 capture is one of the most promising approaches in the CCS field.[9] MOFs are defined as porous crystalline inorganic materials, consisting of metal ions (clusters) that form coordination bonds with organic ligands.[10] The choice of appropriate organic ligands and metal clusters is of crucial importance in the synthesis of MOFs. The replacement of one element gives rise to a different type of MOF, whose structures and properties may be tailored to meet specific applications. Unlike traditional chemical adsorption materials, MOFs offer several advantages, such as high surface area and porosity, large specific pore volumes, lower regeneration costs, and reusability.[11] These properties enable the wide use of MOFs as catalysts,[12,13] drug delivery systems,[14] sensors, and adsorbents.[15–20] The copper benzene-1,3,5-tricarboxylate framework (so-called HKUST-1, Cu-BTC, MOF-199) is one of the most widely studied MOF materials for gas separation and storage, due to its high surface area (600–1600 $m^2\ g^{-1}$), large pore volume, and good thermal stability (stable up to 350 °C).

[a]*The Institute of Nuclear Physics, Ibragimov Str., 1, Almaty, 050032, Kazakhstan. E-mail: i.korolkov@inp.kz*

[b]*L.N. Gumilyov Eurasian National University, Satbaev Str. 5, Astana, 010008, Kazakhstan*

[c]*Department of Chemistry, Hacettepe University, 06800 Ankara, Turkey*

HKUST-1 and its combination with other materials are broadly used in the CCS field. Ho *et al.*[21] describe the solvent-free synthesis of Cu-BTC, and this powder was utilized for carbon dioxide capture. The CO_2 adsorption capacity was 1.7 mmol g^{-1} at 30 °C and showed regenerative ability in up to five adsorption–desorption cycles. The authors[22] demonstrate the influence of graphene-related material (GRM) functionalization on the structural and adsorption performance of HKUST-1. Three types of GRMs, oxidized, hydrazine-reduced, and amine-grafted, were incorporated into the HKUST-1 structure. The modified MOFs demonstrated high surface areas and strong affinities for CO_2 and CH_4.

Significant progress has been made in the development of CO_2 capture membranes, and there has been an increase in the number of publications on the subject over the last 10 years. Numerous studies on CO_2 capture membranes have been published, focusing on their development from a material perspective.[23] These include polymeric,[24,25] mixed-matrix,[26,27] inorganic, MOF,[7] carbon,[28] and electrospun membranes.[29,30] Recently, the development of supported MOF films and membranes has gained considerable attention due to their potential to combine the selectivity of MOFs with the mechanical stability of supporting substrates. The most commonly employed strategies for MOF membrane fabrication involve the use of dense substrates and surface functionalization with organic groups to promote MOF nucleation and growth.[31] In this study,[32] the integration of composite fillers, such as graphene oxide, montmorillonite, and amine-functionalized MOFs, has been shown to significantly enhance membrane selectivity and CO_2 permeability. Hybrid systems offer new opportunities for tuning interfacial interactions, optimizing gas transport pathways, and achieving high-performance gas separation under mild operational conditions. Composite/hybrid membranes combine the advantages of both organic and inorganic components.[23] Various approaches have been explored to produce more effective membranes, including *in situ* growth of MOFs on porous organic polymer templates.[33] However, achieving well-intergrown, free-standing membranes with high MOF concentrations remains a difficult problem. Consequently, there is a growing demand for a new class of porous substrates with easily adjustable structural parameters, including composition, porosity, thickness, size, and, in particular, surface properties. Hazarika and Ingole[34] discussed advancements in polymer-based hollow-fiber membranes and their applicability for industrial gas separation. These works collectively demonstrate the effectiveness of advanced membrane architectures and functional nanomaterials for enhancing CO_2 capture performance.

Techniques such as spray pyrolysis, phase inversion, electrospinning, track-etching, and self-assembly are frequently employed for membrane fabrication.[23] Track-etched membranes (TeMs) are highly versatile and extensively researched materials, and are produced by irradiating polymer films such as poly(ethylene terephthalate) (PET), polycarbonate (PC), polyimide (PI), polypropylene (PP), and poly(vinylidene fluoride) (PVDF).[35] TeMs have several advantages, including narrow pore size distribution, flexibility, small thickness, and chemical compatibility. The structure allows for the tuning of membrane transport properties for various applications, including water filtration, membrane distillation, gas separation, catalysis, and sensor technology.[36–40] Moreover, TeMs can be modified through various functionalization techniques, including electroless, electrochemical and radiochemical deposition, graft polymerization of different monomers, and incorporation of nanoparticles.[41] The use of TeMs as a template for MOFs enables the development of a durable polymeric substrate that stabilizes the fragile crystalline structure of MOFs, protecting it from degradation under external loads. Several studies have reported the use of track-etched membranes as templates for MOF growth.[42,43] Caddeo *et al.* successfully demonstrated the growth of nanoMOFs within PC TeMs using the electrodeposition technique.[43] In another work, the authors[42] synthesized HKUST-1 within PET TeM pores using an automated layer-by-layer dip-coating method, with promising results for gas separation.

In our previous work,[44] a method for synthesizing HKUST-1 on PET TeMs to create a composite membrane for CO_2 capture was developed. HKUST-1 was immobilized by first depositing copper microtubes inside the membrane pores, followed by their conversion into HKUST-1. The resulting composite membranes combined the high porosity and selectivity of MOFs with the mechanical strength and flexibility of TeMs. Nevertheless, despite their high specific area (382 m^2 g^{-1}), the CO_2 adsorption capacity of the composite membranes did not exceed 0.53 $\pm$ 0.03 mmol g^{-1}, which could be attributed to the limited accessibility of the active sites. In the present study, we propose a different approach aimed at improving CO_2 capture efficiency. HKUST-1 was incorporated into PVC nanofibers by electrospinning on PET TeMs. To enhance the concentration of the metal–organic frameworks (MOFs), secondary growth of HKUST-1 was performed. The resulting membrane was successfully tested for carbon dioxide capture. Electrospinning is a simple and versatile method for producing nanofibers with a nanometer diameter.[45] Nanofibers offer several advantages, such as low thickness and internal pore connection, high surface area, and the ability to control their functionality and morphology.[30] Various electrospun nanofibers with integrated MOFs have been developed to adsorb CO_2.[46–48] One of the promising directions in the development of new adsorbents is the use of polymeric materials with hydrophobic properties. Poly(vinyl chloride) (PVC) exhibits high hydrophobicity, making it resistant to high humidity conditions and distinguishing it from many conventional sorbents. This characteristic is potentially beneficial for the development of future CO_2 adsorbents designed to operate in gas streams with high moisture content. Most solid-state adsorbents, including zeolites, aminated mesoporous silicas (MCM-41 and SBA-15), and many MOF (HKUST-1) systems, exhibit hydrophilic properties.[49–53] Additionally, the electrospinning method allows the utilization of non-biodegradable plastics, enabling their use as future adsorbents for CCS.[54–57]

2. Experimental methods

2.1 Materials

Copper(II) nitrate trihydrate ($Cu(NO_3)_2 \cdot 3H_2O$) (98%), benzene-1,3,5-tricarboxylic acid (BTC) (95%), poly(vinyl chloride) (PVC),

N,*N*-dimethylformamide (DMF) (99,9%), ethanol (99,9%), and tetrahydrofuran (THF) (99,9%) were purchased from Sigma-Aldrich. Deionised water (18.2 MΩ) was used to prepare all the solutions.

2.2 Preparation of PET TeMs

PET TeMs were prepared by irradiating Hostaphan® brand PET films (thickness 12 μm, Mitsubishi Polyester Film, Germany) with Kr ions with an average energy of 1.75 MeV per nucleon and an ion fluence of 1.12×10^8 ions per cm^2 using a DC-60 ion accelerator (Astana Branch of the Institute of Nuclear Physics, Kazakhstan). The irradiated polymer film was chemically etched in a 2.2 M NaOH solution at 85 °C. After etching, the samples were rinsed with 5% acetic acid (5 min) and deionised water (10 min) and then stored in air at room temperature. The resulting average pore size of the PET TeMs was ~320 ± 10 nm.

2.3 Synthesis of HKUST-1

The HKUST-1 was synthesized by the solvothermal method according to the previously described procedure.[59] $Cu(NO_3)_2 \cdot 3H_2O$ and BTC (1 : 0.5 ratio) were added to 20 mL of ethanol, deionized water, and DMF in equivalent portions. This solution was then stirred for 25 min and transferred into a 20 mL Teflon autoclave glass. The reaction was performed at 100 °C for 18 hours. The product obtained was then washed with water and ethanol and dried overnight at 80 °C.

2.4 Preparation of PVC/HKUST-1@PET TeMs

HKUST-1 (1 wt%) was dissolved in THF and DMF with a weight ratio of 1 : 1 and ultrasonicated for 40 min. The solution mixture was then stirred and heated to 45 °C. PVC (15 wt%) in THF was added to the mixture and stirred. The mixing process was carried out for 24 hours, forming a viscous hybridized solution of PVC/HKUST-1. In a typical electrospinning process, the hybridized solution was pumped using a syringe pump (volume of 10 mL) at a flow rate of 0.5 mL h^{-1}. The applied voltage was kept at 15.5 kV, the distance between the needle tip and PET TeMs in the collector was 15 cm. PVC/HKUST-1@PET TeMs were dried at 60 °C.

2.5 Secondary decoration of MOFs

The obtained PVC/HKUST-1@PET TeM was subjected to MOFs secondary decoration (SD) using the solvothermal method. In order to achieve this, a solution of $Cu(NO_3)_2 \cdot 3H_2O$ and BTC was prepared by following the above method. Three different solutions with $Cu(NO_3)_2 \cdot 3H_2O$ and BTC mole ratio 1 : 0.5 were prepared. The PVC/HKUST-1@PET TeMs obtained by electrospinning were placed into a Teflon autoclave glass containing the solutions of $Cu(NO_3)_2 \cdot 3H_2O$ and BTC. The reaction was performed at 100 °C for 24 hours. Upon completion of the reaction, the membrane was washed with water and ethanol and dried at 80 °C for 5 hours. The resulting precipitate was centrifuged, washed with ethanol and deionized water, and dried at 80 °C for 12 hours. The general scheme for the preparation of PVC/HKUST-1 (SD)@PET TeMs is shown in Fig. 1.

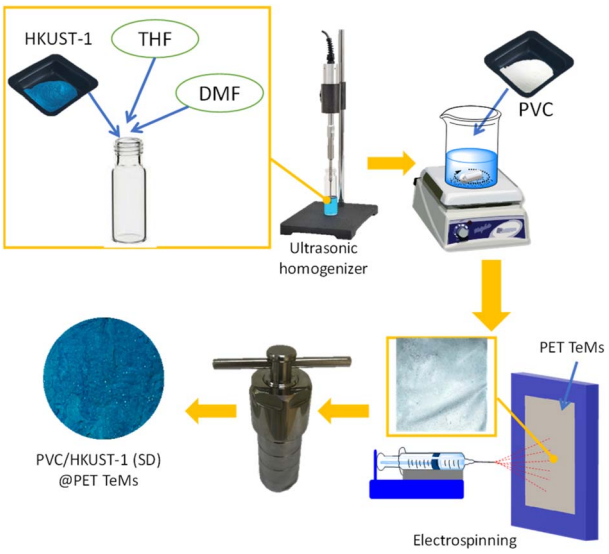

Fig. 1 Schematic of the preparation of PVC/HKUST-1 (SD)@PET TeMs.

2.6 Characterization techniques

Fourier transform infrared (FTIR) spectroscopy was performed using an InfraLUM FT-08 spectrometer equipped with a variable angle specular reflectance accessory (VeeMax™ III, PIKE, USA). Spectra were recorded in the range of 400–4000 cm^{-1} with 25 scans, and a resolution of 2 cm^{-1}. This analysis was conducted to evaluate chemical changes before and after modification.

The pore size of the TeMs was measured by the gas flow rate method at a pressure of 20 kPa.

A Hitachi TM 3030 scanning electron microscope (SEM) with an energy-dispersive X-ray spectroscopy (EDX) system (Bruker XFlash MIN SVE) at an accelerating voltage of 15 kV was utilized for studying the morphology and elemental composition of the samples. The results of the analysis are presented as averages based on three data points.

X-ray diffractograms (XRD) were recorded at room temperature with a Rigaku SmartLab diffractometer. A Cu-Kα copper tube ($\lambda = 1.5406$ Å) was used as the X-ray source. The diffractograms were recorded in Bragg–Brentano geometry (θ–θ scan) with a step of 0.025° and a speed of 3° per min. The diffractograms were analyzed using DiffracEva V.4.2.1 software.

The thermal stability of the samples was tested by using a Themys One + thermogravimetric analyzer (Setaram Instrumentations, Caluire, Switzerland). Each sample was measured within the temperature range from 25 °C to 600 °C, at a heating rate of 10°C min^{-1} in a continuous flow of pure Ar gas.

A Brunauer–Emmett–Teller (BET) instrument (V-Sorb 2800P BET surface area and porosity analyzer, Gold App Instruments Corp., Xi'an, China) was used to determine the specific surface area, total pore volume, and pore size distribution of the samples based on N_2 adsorption–desorption isotherms. The mesopore size distribution was calculated using the BJH method, and the micropore size distribution was calculated by DFT kernel fitting (carbon slit) using pyGAPS.[60]

The wetting properties were measured using a digital microscope with 1000× magnification at room temperature. The water contact angle (CA) was evaluated using the static drop method. The analysis was repeated five times at different positions. The CA was determined by using the ImageJ program with Drop Analysis-Drop Snake plugins. The calculation of specific surface energy from the CA measurements is based on the Owens, Wendt, Rabel and Kaelble (OWRK) method, using CA with two liquids – polar and dispersive. DI water was used as the polar protic liquid, and diiodomethane was used as the nonpolar aprotic liquid. The surface energy of the solid (γ_s) was calculated as the sum of the dispersive (γ_S^d) and polar (γ_S^p) components using the OWRK eqn (1):

$$\gamma_L \times (1 + \cos\theta) = 2\left(\sqrt{\gamma_S^p \times \gamma_L^p} + \sqrt{\gamma_S^d \times \gamma_L^d}\right) \quad (1)$$

where θ is the measured CA, and γ_L^d and γ_L^p are the dispersive and polar components of surface tension, respectively.

2.7 CO_2 adsorption/desorption

The CO_2 adsorption capacities were measured by using the TGA apparatus at different temperatures and a gas pressure of 0.1 MPa. The adsorption test was conducted in two steps: degasification and adsorption. The sample (15 mg) was placed in the TGA sample holder, and the temperature was increased to 150 °C at a heating rate of 10°C min^{-1} to remove the solvent over 60 min. The sample was then cooled to 25 °C. The adsorption test began by switching the gas flow to CO_2 and continued for 2 hours until saturation. The adsorption capacity (AC) for each membrane was calculated by using equation (S1) (see the SI). In the desorption test, Ar was used to purge the adsorbed CO_2 in the membrane at an elevated temperature of 150 °C. The adsorption followed by the desorption process was repeated in 12 cycles to examine the regeneration ability of the sample. The sorption-desorption cycles were performed for 2 h (1 h sorption and 1 h desorption). The regenerative (q) properties in percentage were determined by using equation (S2) (see the SI).

3. Results and discussion

3.1 Characterization of HKUST-1

Many methods have been reported for the synthesis of HKUST-1, including hydrothermal and solvothermal methods, microwave-assisted, sonication, and electrochemical methods.[61–64] The solvothermal method of HKUST-1 powder production was chosen.[59] The synthesis of HKUST-1 is illustrated in Fig. 2. The coordination during the synthesis of HKUST-1 was based on the formation of coordination bonds between copper ions (Cu^{2+}) and the organic ligand benzene-1,3,5-tricarboxylate (BTC). During synthesis, Cu^{2+} ions assemble into dimeric secondary building units known as paddlewheel clusters, in which each pair of copper centers is bridged by four carboxylate groups.[65] Further connection of these units with BTC linkers results in the construction of a three-dimensional porous crystalline framework.[66,67] In the as-

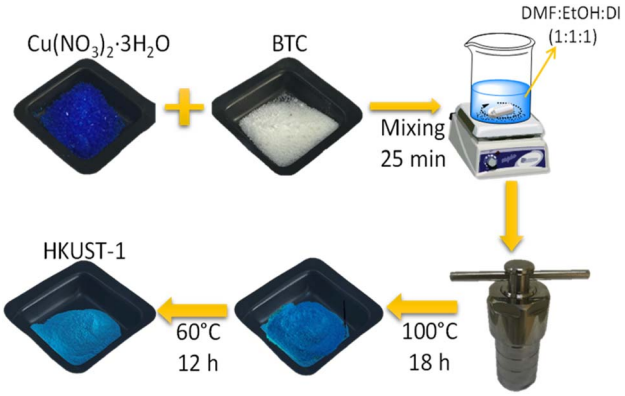

Fig. 2 Synthesis of the HKUST-1.

synthesized state, the axial position of copper atoms is typically occupied by water or solvent molecules, which can be removed upon activation. This process generates open metal sites with Lewis acidic nature, which play a crucial role in the adsorption of various gases.[68]

The structural characteristics of the prepared HKUST-1 were determined by using SEM-EDX, N_2 adsorption–desorption, and XRD techniques. The SEM images of the synthesized HKUST-1, shown in Fig. 3, exhibit typical hexagonal and octahedral morphology with a particle size of about 10–20 μm, as reported elsewhere. The elemental composition (Fig. 3b) of the membrane surface was studied by EDX, which showed a carbon content of 36.2% ± 0.07%, oxygen 33.7% ± 0.07% and copper 29.5% ± 0.5%.

Fig. 4a presents the N_2 adsorption–desorption isotherm. Synthesized HKUST-1 shows a typical type-I isotherm, revealing its microporous nature, which is consistent with the literature data.[69,70] The BET surface area was determined to be 813.12 m^2 g^{-1}, and the median pore size was 0.85 nm.

The specific surface energy of HKUST-1 was 75.72 mN m^{-1} by the OWRK model. Differences in the measured BET surface areas and pore volumes reported in various studies can often be explained by variations in post-synthesis treatment procedures, such as the washing steps and activation methods applied to the HKUST-1 samples, or an increase in the number of defects in the lattice.[69,71]

The XRD pattern (Fig. 4c) displayed strong diffraction peaks, which can be attributed to the cubic structure with the *Fm*-3*m* space group of HKUST-1 (PDF 00-065-1028). The patterns obtained for pure Cu-BTC were assigned to the specific phase peaks, which are consistent with the literature data.[72] The XRD pattern of the synthesized HKUST-1 exhibits a series of sharp and intense peaks at 2θ values of 6.5°, 9.5°, 11.5°, 12.5°, and 13.4°, in agreement with our study, indicating a highly crystalline structure. The most intense peak at around 9.5° is characteristic of HKUST-1 and corresponds to the specific crystallographic (220) plane reported for the standard HKUST-1 phase.[63,66]

The FTIR spectra of the synthesized HKUST-1 are shown in Fig. 4b. The peaks between 1650 cm^{-1} and 1374 cm^{-1} are

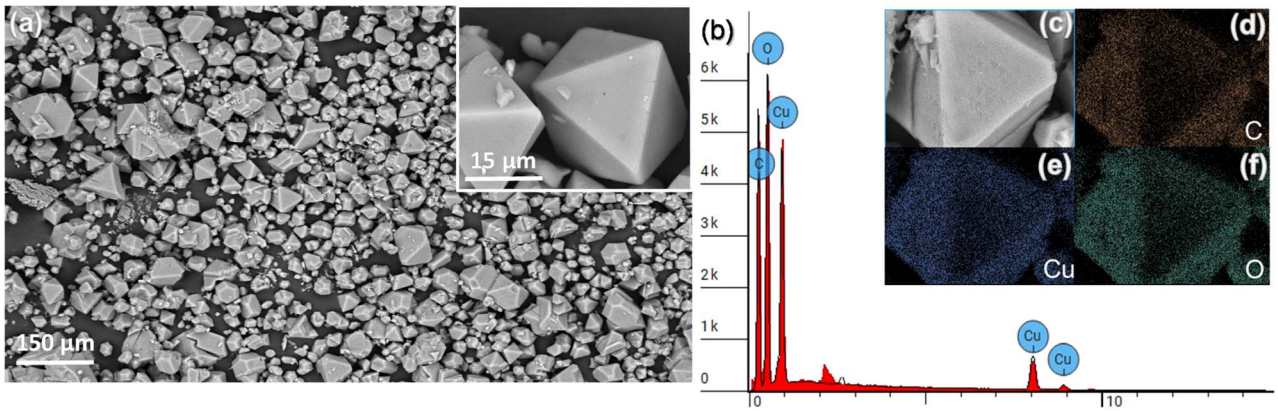

Fig. 3 SEM images of HKUST-1 in different magnifications (a and c); EDX spectra (b) and distribution of carbon (d), copper (e) and oxygen (f) on the MOF surfaces.

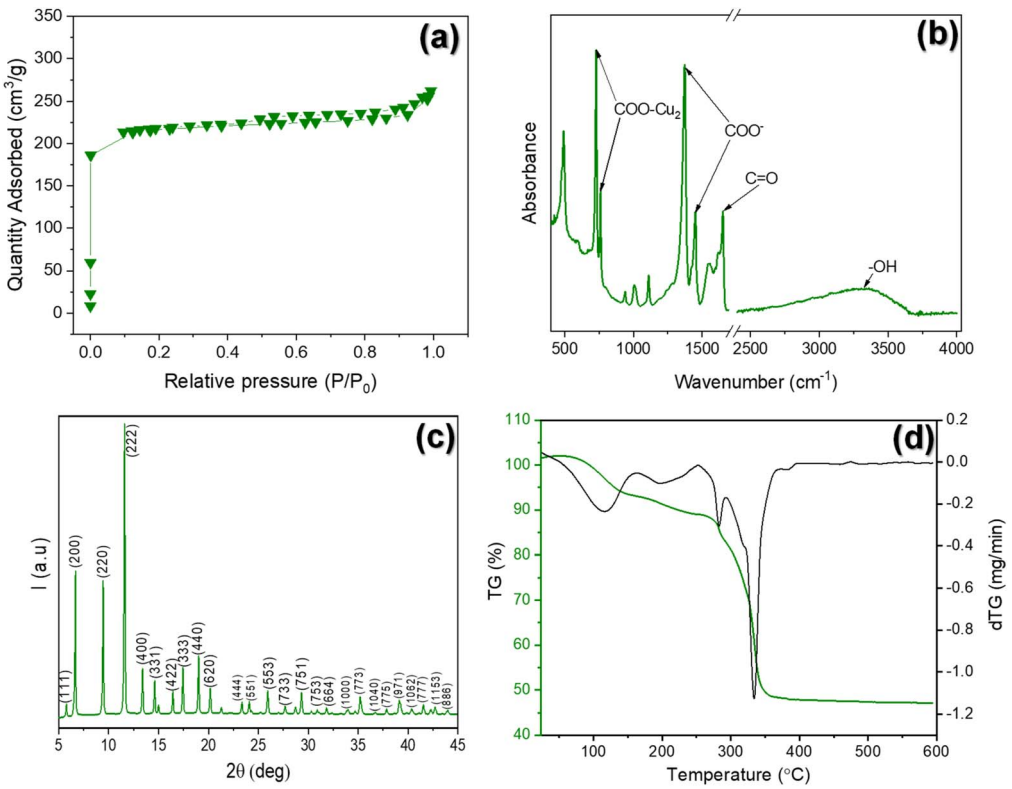

Fig. 4 N_2 adsorption–desorption isotherms (a), FTIR spectrum (b), XRD pattern (c) and thermogram of the synthesized HKUST-1 (d).

attributed to the bidentate coordination of asymmetric and symmetric carboxylate ligands, indicating the organization of BTC with the copper sites.[73] Also, peaks at 780 cm^{-1} and 724 cm^{-1} indicate the coordination of the O atom with Cu (Cu–O bond). Fig. 4d shows the thermogram of HKUST-1 synthesised by the solvothermal method. The thermogram shows a weight loss with increasing temperature. In the first step, a weight decrease at around 66 °C is observed, which indicates the evaporation of solvent molecules adsorbed on the surface. Then, in the range of 150 to 250 °C, a weight loss of 2.03% was observed, which is probably due to the removal of chemisorbed water in the MOF structure, since the synthesis was carried out in a mixture of solvents, one of which was water. The HKUST-1 was expected to be quite thermally stable. The decomposition of organic ligands in the MOF structure was observed at around 340 °C, with a weight loss of 46.1%. Subsequently, the residue remained stable starting from 350 °C as CuO.[74]

3.2. Characterization of the membrane

Electrospinning technology makes it possible to obtain membranes with a rough and porous single-fiber structure and a homogeneous distribution of MOF particles. The use of a PET

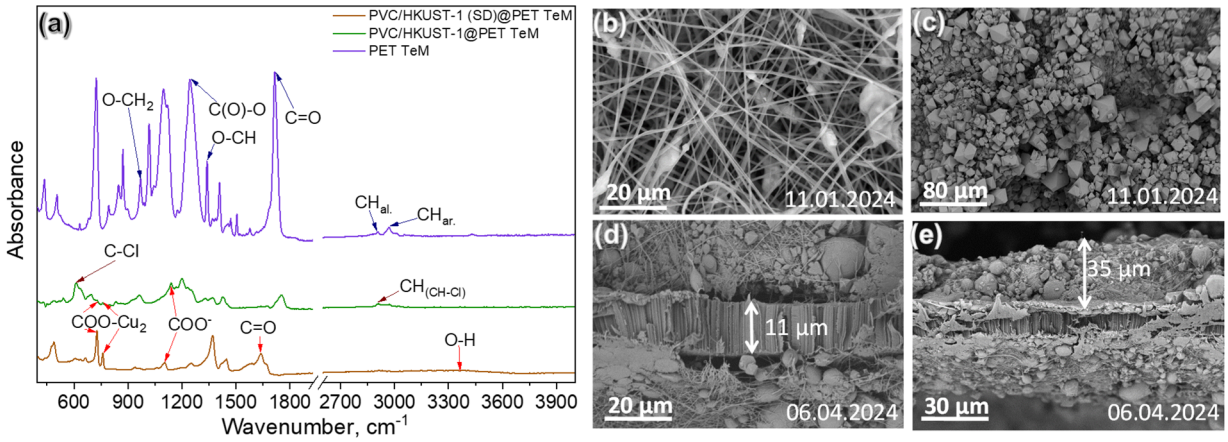

Fig. 5 FTIR spectra of the unmodified and modified PET TeMs (a); SEM images of the PVC/HKUST-1@PET TeM before (b) and after (c) secondary decoration and a cross-section of the PVC/HKUST-1(SD)@PET TeM (d and e).

TeM template helps to create a self-supporting and flexible membrane. As shown in Fig. 1, the fabrication process begins with the PVC/HKUST-1@PET TeM skeleton. The HKUST-1 particles embedded in the electrospun PVC serve as uniform and stable seed crystals for the secondary growth of the MOF. Each modification step of the samples was followed by FTIR spectroscopy. The results are presented in Fig. 5. The FTIR spectrum of the initial PET TeM shows characteristic peaks at 2970 cm^{-1} (CH aromatic), 2915 cm^{-1} (C–H aliphatic), 1710 cm^{-1} (C=O), 1615, 1468, 1428, 1409 cm^{-1} (aromatic ring vibrations), 1340 cm^{-1} (O–CH_2), and 1240 cm^{-1} (C(O)–O).[37] The typical FTIR spectrum of PVC is observed after the deposition of PVC/HKUST-1 nanofibers on the PET TeM surface, which is consistent with the literature data.[75]

The characteristic vibrations of PVC can be divided into 3 regions. The first region includes C–Cl vibrations (610 cm^{-1}, 691 cm^{-1}), and the second region includes C–C and C–H_2 (1333 cm^{-1}). The third region corresponds to CH– vibrations (2970–2929 cm^{-1}).[76] After secondary growth of MOFs, the FTIR spectra revealed characteristic bonds associated with HKUST-1. Peaks from 1635 cm^{-1} to 1374 cm^{-1} correspond to COO^- vibrations, indicating also a bidentate coordination mode. In addition, new peaks at 780 cm^{-1} and 724 cm^{-1} reflect the coordination of oxygen atoms with Cu (Cu–O). The intensity of these peaks increased, and a small peak at 3375 cm^{-1} (OH groups) appeared after the secondary decoration of HKUST-1.[74,77]

The morphological structure of the PET TeM based material was examined using SEM, and the results are presented in Fig. 5b–e. The electrospun PVC/HKUST-1 nanofibers exhibited a light bluish-white color (Fig. S4). The SEM images show a chaotic distribution of nanofibers with an average outer diameter of 0.16 ± 0.04 µm. Additionally, visible MOF inclusions can be observed, which are beneficial for the secondary growth process. After secondary decoration, a noticeable increase in MOF crystal size on the membrane surface was detected. The cross-sectional view of the PVC/HKUST-1(SD)@PET TeMs is presented in Fig. 5d–e. The PVC/HKUST-1 mat obtained has a thickness of 35 µm, with the electrospun and secondary grown layer tightly adhered to the PET TeMs. The elemental composition of the membrane surface was studied by EDX. According to the EDX results, the copper and chlorine concentrations after the electrospinning process were 1.0% ± 0.04% and 10.9% ± 3.3%, respectively. After the secondary decoration of the samples, an increase in surface Cu concentration (29.3% ± 2.8%) and a decrease in chlorine concentration (1.8% ± 0.28%) were observed.

Compared to other adsorbents for CO_2 capture, one of the key characteristics of PVC-based materials is their hydrophobicity. Hydrophobic adsorbents are particularly beneficial in environments with high moisture content, such as in flue gas. To assess the hydrophobic properties of the membrane, an experiment was conducted to measure the CA of water droplets on its surface. Fig. 6 shows the results of CA measurements on the membrane. The PET TeMs have hydrophilic properties, and water can easily pass through the pores of the membrane (CA = 51° ± 3°). After the deposition of PVC/HKUST-1 nanofibers by

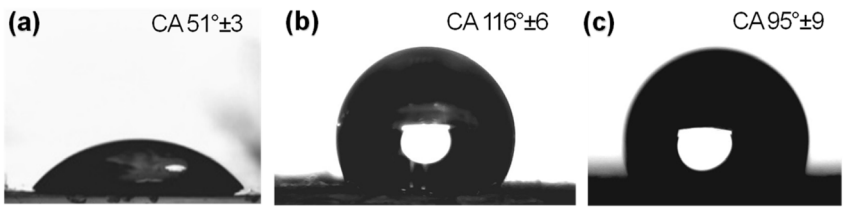

Fig. 6 The CAs of the pristine PET TeM (a), PVC/HKUST-1@PET TeM (b) and PVC/HKUST-1(SD)@PET TeM (c).

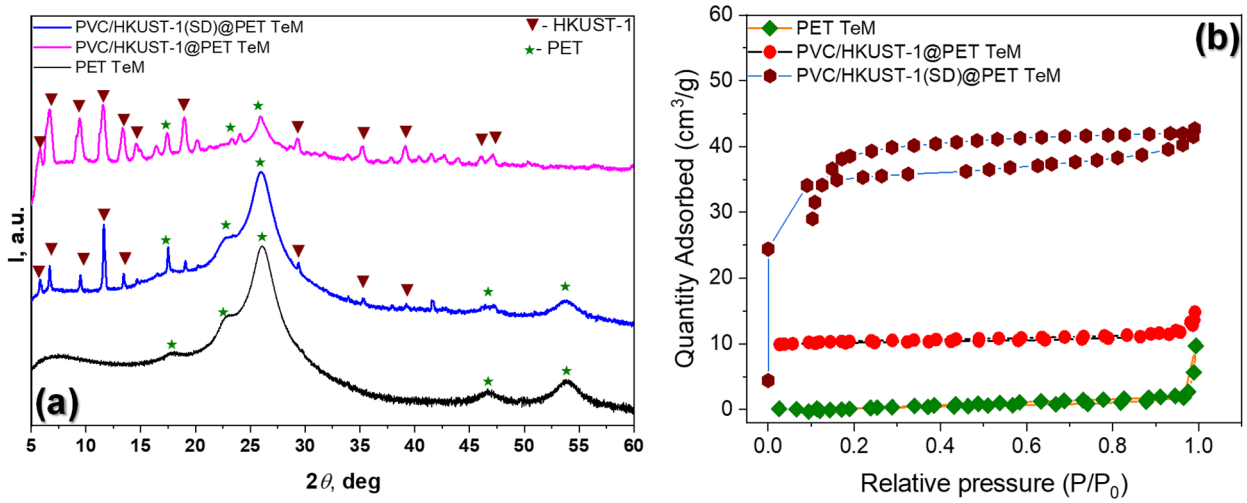

Fig. 7 (a) Comparison of the XRD patterns of the PVC/HKUST-1@PET TeM composite samples and (b) N_2 adsorption–desorption isotherms of the samples.

the electrospinning method, the CA increased to 116° ± 6°. This is due to the hydrophobicity of PVC (CA = 145°).[75] The decrease in the CA of PVC/HKUST-1 (SD)@PET TeM is due to the hydrophilic nature of HKUST-1. After secondary decoration of MOFs in the membrane, the CA was 95° ± 9°. The ability to regulate the hydrophobic–hydrophilic balance plays a significant role, as it can increase the stability of compounds and enhance the adsorption capacity for CO_2 capture. Despite the high contact angle observed for the modified membrane, experimental studies demonstrated that its gas permeability remained high. Tests confirmed that air can pass freely through the membrane, indicating that the PVC nanofiber layer does not negatively affect gas transport. The surface energy of the composite membranes was determined using the OWRK model based on CA measurements with water and diiodomethane. Pristine PET TeM exhibited a total surface energy of 48.26 mJ m^{-2}, dominated by the polar component, confirming its hydrophilic nature. After incorporation of HKUST-1 particles into the PVC@PET TeM, the surface energy was 48.73 mN m^{-1}. The membrane with secondary decoration showed a surface energy of 55.69 mN m^{-1}, indicating enhanced surface polarity and improved interaction with polar substances, such as CO_2.[78,79]

The XRD pattern of the samples is shown in Fig. 7a. The pristine PET TeMs have a semi-crystalline structure with broad peaks, which were identified by using the PDF (00-061-1413). Fig. 8a shows a comparison of the patterns of the composites and the original components. PVC/HKUST-1@PET TeMs composites have sets of Bragg peaks from PET and HKUST-1, namely (111), (200), (222), (400), (331), (420), (422), (333), (440), and (442), and the main PET peaks from (100), (110), and (230). Peaks from other phases were not found in the composites, indicating that new crystalline phases were not formed during the synthesis. As the concentration of HKUST-1 increases, peaks from (751), (773), (971), and (777) were also observed. During the synthesis of the composites, it can be

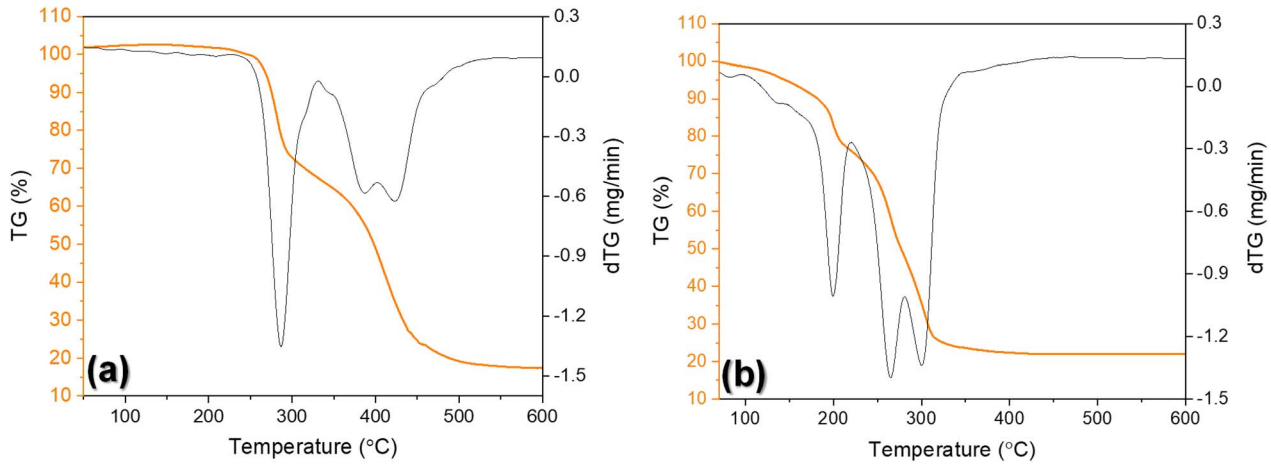

Fig. 8 Thermal degradation plots of (a) the PVC@HKUST-1/PET TeM and (b) PVC@HKUST-1 (SD)/PET TeM.

Table 1 Results of BET analyses

Sample	BET surface area ($m^2 g^{-1}$)	Langmuir surface area ($m^2 g^{-1}$)	BJH[a] adsorption average pore width (nm)	BJH adsorption cumulative volume ($cm^3 g^{-1}$	DFT[a] median pore width (nm)	DFT total pore volume ($cm^3 g^{-1}$)
PET TeM	1.72	2.58	30.85	0.017	—	—
PVC@PET TeM	2.08	5.61	35.66	0.016	—	—
PVC/HKUST-1@PET TeM	1.97	3.10	20.24	0.007	8.84	0.003
PVC/HKUST-1 (SD)@PET TeM	135.26	148.77	—	—	0.84	0.050
HKUST-1	813.12	928.39	—	—	0.85	0.306

[a] BJH – Barrett–Joyner–Halenda; DFT-density functional theory.

Table 2 Effect of temperature on CO_2 capture

Temperature	25 °C	30 °C	50 °C	80 °C
AC, mmol g^{-1}	1.48	1.24	0.53	0.23

observed that there is no change in the lattice parameters of the cubic structure of HKUST-1 compared to the original powder.[80]

The specific surface area and pore size of the samples were studied by using N_2 adsorption–desorption isotherms, and the results are presented in Fig. 7b and Table 1. The specific surface area and Langmuir surface area of HKUST-1 were found to be significantly higher than those of the composite samples, indicating its strong sorption capacity. For mesoporous samples, the average pore diameter and cumulative pore volume were calculated using the BJH model; for microporous samples, the median pore diameter and total pore volume were determined using DFT (carbon slit kernel, pyGAPS). The PVC/HKUST-1@PET TeM sample was analyzed using both methods, as its adsorption behavior is dominated by mesopores, as evidenced by its Type IV isotherm. A minor contribution from HKUST-1 is also present, as indicated by the pore size distribution curve (Fig. S2c), which shows pores in the 1–8 nm range. The PVC/HKUST-1(SD)@PET TeM sample exhibits a Type I adsorption isotherm, which is consistent with the behavior observed for the HKUST-1 sample. Mesopore/micropore pore size distributions for all the samples are presented in Fig. S2 (see the SI).

Fig. 8a shows that thermal degradation of the PVC/HKUST-1@PET TeM sample also occurs in 3 stages. The first stage involves dehydrochlorination of the PVC with ~35% weight loss, and the second stage leads to degradation of the organic ligands of MOF.[81] The last stage involves chain breaking of the PET TeM up to a temperature of 432 °C.[75] After secondary growth, the membrane is observed to degrade in three stages (Fig. 8b). The first stage is the release of bound and free water around 200 °C. Then, dehydrochlorination of the PVC nanofibers takes place at around 250 °C and 350 °C to 420 °C, leading to the destruction of the organic structure. The residue remained stable starting from 432 °C as CuO.

3.3 CO_2 adsorption performance

The carbon dioxide adsorption and desorption on the PVC/HKUST-1(SD)@PET TeMs were measured using a TGA apparatus. The CO_2 adsorption performance of the obtained membrane was evaluated at different temperatures (Table 2 and Fig. S3).

According to the results, the adsorption capacity decreased from 1.48 mmol g^{-1} to 0.23 mmol g^{-1} with the increase in the adsorption temperature. Based on literature reports, the initial adsorption of carbon dioxide predominantly occurs at exposed copper cations and within the framework windows of the structure. These positively charged copper sites are regarded as the primary adsorption centers for CO_2 molecules. Subsequent CO_2 adsorption is largely driven by van der Waals forces; however, the electrostatic interactions between the copper sites

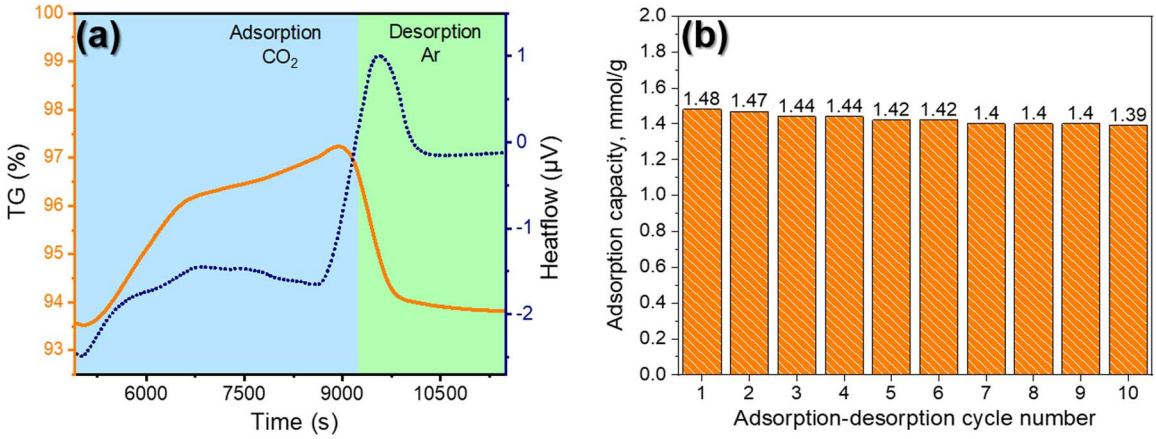

Fig. 9 (a) CO_2 adsorption/desorption plots of the PVC/HKUST-1 (SD)@PET TeM and (b) CO_2 adsorption capacity after each cycle for the PVC/HKUST-1 (SD)@PET TeM.

and the quadrupole moment of CO_2 are substantially stronger than conventional van der Waals interactions, thereby playing a crucial role in enhancing the overall adsorption affinity.[82–84] The CO_2 adsorption/desorption plots of PVC/HKUST-1 (SD)@PET TeM are presented in Fig. 9a. The adsorption capacity of the obtained membrane was 1.48 mmol g^{-1}.

Testing of the membranes for CO_2 adsorption–desorption was carried out to evaluate their reversibility and regenerative ability, and the relevant results are shown in Fig. 9b. After each adsorption test, desorption was performed by raising the temperature to 150 °C and purging with Ar gas. After 12 cycles of regeneration, the carbon dioxide adsorption capacity for PVC/HKUST-1(SD)@PET TeM was found to decrease from 1.48 mmol g^{-1} to 1.39 mmol g^{-1}, a reduction of ~6% in performance. This means that up to 94% of the CO_2 adsorption capacity can be maintained after 12 adsorption–desorption cycles. To assess the long-term stability of the membrane, samples were stored under ambient conditions for three months. The CO_2 adsorption capacity decreased by 0.5%, a value within the measurement error, thereby confirming that the membrane retains its structural integrity and functional performance over time.

The performance of our composite membrane was compared with those of other HKUST-containing membranes, as presented in Table 3. As can be seen, the PVC/HKUST-1(SD)@PET TeM shows a medium CO_2 adsorption capacity compared to some other membranes. Although the CO_2 adsorption capacity of the HKUST-1 powder (1.62 mmol g^{-1}) is higher than that of PVC/HKUST-1(SD)@PET TeM, which is due to the significantly lower concentration of HKUST-1 on the hybrid membrane, the use of the composite membrane may have advantages such as flexibility and robustness, and provides the possibility of distributing HKUST-1 throughout the branched structure of the membrane.

Table 3 Some HKUST-based membranes and their CO_2 adsorption capacity

No.	Membrane	AC, mmol g^{-1}	Ref.
1	PAN/HKUST@HKUST-1-3A NFM	3.9	47
2	PAN/HKUST-1 mats	2.55	85
3	HKUST-1-coated foam	0.4	86
4	Core/shell Nylon 6.6/La-TMA	0.219	87
5	KTA@HKUST-1-10	3.6	88
6	EDA-PVC/SBA-15	0.54	58
7	HKUST-1	1.62	This study
8	PVC/HKUST-1(SD)@PET TeMs	1.48	This study

Various kinetic models have been proposed to describe the adsorption processes of different adsorbents. Among them, the pseudo-first-order and pseudo-second-order models are the most commonly applied. Both of the kinetic models are applicable to gas–solid adsorption reactions on porous adsorbents. In our study, these models were used to analyze the CO_2 adsorption behavior of the obtained membranes.

Fig. 10 presents the adsorption curve of the PVC/HKUST-1(SD)@PET TeM along with the linear curve obtained from pseudo-first-order and pseudo-second-order models. The adsorption capacity is plotted as a function of time up to 350 min. The pseudo-first-order kinetic model is among the early models of sorption kinetics, describing the reversible interaction between absorbent and adsorbate, which is suitable for physical adsorption.[89] The pseudo-second-order kinetic model is mostly used to describe the chemical adsorption.[90,91] Table 4 shows the parameters of kinetic models at 25 °C along with the correlation coefficient (R^2).

It can be seen from Table 4 that the pseudo-second-order model gives a more acceptable fit, with $R^2 = 0.9786$. The membrane demonstrates an adsorption capacity of $q_e = 2.84$ mmol g^{-1} and rate constant $k_2 = 0.22 \times 10^{-5}$ g (mg^{-1} min^{-1}). According to our results, it can be assumed that chemisorption predominates on the PVC/HKUST-1(SD)@PET TeM. This conclusion is consistent with literature reports, where adsorption on HKUST-1 is described as a chemisorption process depending on the structural characteristics.[88,89]

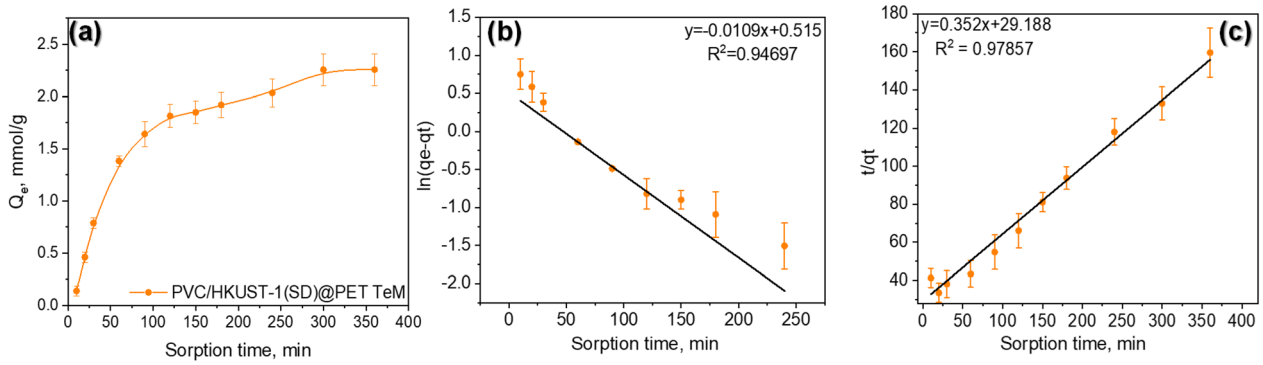

Fig. 10 (a) CO_2 uptake kinetics of the PVC/HKUST-1(SD)@PET TeM and linear curve adsorption kinetics according to the pseudo-first-order (b) and pseudo-second-order (c) kinetic models.

Table 4 Kinetic parameters for CO_2 capture on the PVC/HKUST-1(SD)@PET TeM

Kinetic model	Parameters	
Pseudo-first order	$k_1 \times 10^{-5}$, min^{-1}	4.54
	q_e, mmol g^{-1}	1.67
	R^2	0.9469
Pseudo-second order	$k_2 \times 10^{-5}$, g mg^{-1} min^{-1}	0.22
	q_e, mmol g^{-1}	2.84
	R^2	0.9786

4 Conclusions

In conclusion, our study demonstrates a successful approach to fabricating membranes for carbon dioxide capture by integrating HKUST-1 in PET TeMs using electrospun PVC/HKUST-1 mats as seed layers for secondary MOF growth. Comprehensive characterization confirmed the uniform MOF distribution and the structural integrity of the material. The resulting PVC/HKUST-1(SD)@PET TeMs showed a CO_2 adsorption capacity of 1.48 mmol g^{-1} at 25 °C, with a cyclic stability of 94%, indicating strong potential for applications in CO_2 capture.

Author contributions

A. Kh. Sh.: investigation, writing – original draft, data curation, visualization; D. D. O. – investigation, data curation; Zh K. Zh.: supervision, writing review and editing; R. I. Sh., A. T. Zh.: investigation, data curation; O. G.: conceptualization, supervision, writing review and editing; and I. V. K.: conceptualization, supervision, writing review and editing, project administration, funding acquisition.

Conflicts of interest

The authors declare no competing interests.

Data availability

All data generated in this study are available in the article and the SI. Supplementary information is available: corresponding data files for BET, FTIR, XRD, TGA analyses. See DOI: https://doi.org/10.1039/d5ra04733a.

Acknowledgements

This work was carried out with the financial support of the Ministry of Science and Higher Education of the Republic of Kazakhstan (grant No. AP19676702). In preparing this manuscript, authors utilized Grammarly and ChatGPT to enhance the English grammar and style for improved clarity and readability. The original draft and subsequent revisions were written by authors themselves. Following the use of these tools, the authors thoroughly reviewed and edited the output and assumed full responsibility for the final content of this publication.

References

1 E. R. J. H. Dunn, F. Aldred, N. Gobron, J. B Miller and K. M. Willett, *Bull. Am. Meteorol. Soc.*, 2022, **103**, S11–S142.
2 O. Güven and B. S. Han, *Radiat. Phys. Chem.*, 2022, **198**, 110282.
3 D. Y. C. Leung, G. Caramanna and M. M. Maroto-Valer, *Renew. Sustain. Energy Rev.*, 2014, **39**, 426–443.
4 S. Acevedo, L. Giraldo and J. C. Moreno-Piraján, *ACS Omega*, 2020, **5**, 10423–10432.
5 D. G. Boer, J. Langerak and P. P. Pescarmona, *ACS Appl. Energy Mater.*, 2023, **6**, 2634–2656.
6 S. M. Amaraweera, C. A. Gunathilake, O. H. P. Gunawardene, R. S. Dassanayake, E. B. Cho and Y. Du, *Nanomater.*, 2023, **13**, 2050.
7 Q. Qian, P. A. Asinger, M. J. Lee, G. Han, K. Mizrahi Rodriguez, S. Lin, F. M. Benedetti, A. X. Wu, W. S. Chi and Z. P. Smith, *Chem. Rev.*, 2020, **120**, 8161–8266.
8 O. H. P. Gunawardene, C. A. Gunathilake, K. Vikrant and S. M. Amaraweera, Carbon dioxide capture through physical and chemical adsorption using porous carbon materials: a review, *Atmosphere*, 2022, **3**(13), 397.
9 M. Ding, R. W. Flaig, H. L. Jiang and O. M. Yaghi, *Chem. Soc. Rev.*, 2019, **48**, 2783–2828.
10 L. Hu, V. T. Bui, N. Esmaeili and H. Lin, *Carbon Capture Sci. Technol.*, 2024, **10**, 100150.

11 H. Demir, G. O. Aksu, H. C. Gulbalkan and S. Keskin, *Carbon Capture Sci. Technol.*, 2022, **2**, 100026.
12 T. Saeed, A. Naeem, I. U. Din, M. Farooq, I. W. Khan, M. Hamayun and T. Malik, Synthesis of chitosan composite of metal-organic framework for the adsorption of dyes; kinetic and thermodynamic approach, *J. Hazard. Mater.*, 2022, **427**(5), 127902.
13 J. Liu, T. A. Goetjen, Q. Wang, J. G. Knapp, M. C. Wasson, Y. Yang, Z. H. Syed, M. Delferro, J. M. Notestein, O. K. Farha and J. T. Hupp, *Chem. Soc. Rev.*, 2022, **51**, 1045–1097.
14 I. Abánades Lázaro, X. Chen, M. Ding, A. Eskandari, D. Fairen-Jimenez, M. Giménez-Marqués, R. Gref, W. Lin, T. Luo and R. S. Forgan, *Nat. Rev. Methods Prim.*, 2024, **41**(4), 1–20.
15 X. Xu, Q. Wei, Z. Xi, D. Zhao, J. Chen, J. Wang, X. Zhang, H. Gao and G. Wang, *Coord. Chem. Rev.*, 2023, **495**, 215393.
16 L. Li, H. S. Jung, J. W. Lee and Y. T. Kang, *Renew. Sustain. Energy Rev.*, 2022, **162**, 112441.
17 M. Zhao, Y. Yang and X. S. Gu, *Inorg. Chem. Commun.*, 2023, **152**, 110722.
18 S. Mahajan and M. Lahtinen, *J. Environ. Chem. Eng.*, 2022, **10**, 108930.
19 R. Lalawmpuia, M. Lalhruaitluangi, Lalhmunsiama and D. Tiwari, Metal organic framework (MOF): Synthesis and fabrication for the application of electrochemical sensing, *Environ. Eng. Res.*, 2024, **29**(5), 230636.
20 L. Fu, Z. Ren, W. Si, Q. Ma, W. Huang, K. Liao, Z. Huang, Y. Wang, J. Li and P. Xu, *J. CO_2 Util.*, 2022, **66**, 102260.
21 P. S. Ho, K. C. Chong, S. O. Lai, S. S. Lee, W. J. Lau, S. Lu and B. S. Ooi, *Aerosol Air Qual. Res.*, 2021, **22**, 1–14.
22 V. Gargiulo, F. Raganati, P. Ammendola, M. Alfe and R. Chirone, *Chem. Eng. Trans.*, 2015, **43**, 1087–1092.
23 G. Hazarika and P. G. Ingole, *Sci. Total Environ.*, 2024, **944**, 173264.
24 Y. Han and W. S. W. Ho, *Chinese J. Chem. Eng.*, 2018, 2238–2254.
25 Z. Dai, L. Ansaloni and L. Deng, *Green Energy Environ.*, 2016, **1**, 102–128.
26 Z. Yang, Z. Wu, S. Bo, Y. Ying, H. Yang and D. Zhao, *Engineering*, 2023, **23**, 40–55.
27 Z. Qin, Y. Ma, J. Wei, H. Guo, B. Wang, J. Deng, C. Yi, N. Li, S. Yi, Y. Deng, W. Du, J. Shen, W. Jiang, L. Yao, L. Yang and Z. Dai, *Green Energy Environ.*, 2024, **9**, 831–858.
28 S. Zirak, H. Kiadeh, A. Ghaee, M. Farokhi, J. Nourmohammadi, A. Bahi and F. K. Ko, *Int. J. Biol. Macromol.*, 2021, **173**, 351–365.
29 K. Allmond, J. Stone, S. Harp, K. Mujibur and Wahiduzzaman, Synthesis and Electrospraying of Nanoscale MOF (Metal Organic Framework) for High-Performance CO_2 Adsorption Membrane, *Nanoscale Res. Lett.*, 2017, **12**(6), DOI: 10.1186/s11671-016-1798-6.
30 X. Wang and B. Li, Electrospun Nanofibrous Sorbents and Membranes for Carbon Dioxide Capture, in *Electrospun Nanofibers for Energy and Environmental Applications*, ed. B. Ding and J. Yu, Nanostructure Science and Technology, Springer, Berlin, Heidelberg, 2014, DOI: 10.1007/978-3-642-54160-5_10.
31 R. Chen, M. Chai and J. Hou, *Carbon Capture Sci. Technol.*, 2023, **8**, 100130.
32 G. Hazarika, S. Goswami, M. Borpatra Gohain and P. G. Ingole, Effect of Different Nanofillers in Mixed Matrix Membranes for CO_2 Separation, *ACS Appl. Polym. Mater.*, 2025, **7**(1), 148–163.
33 J. Yu, L. H. Xie, J. R. Li, Y. Ma, J. M. Seminario and P. B. Balbuena, *Chem. Rev.*, 2017, **117**, 9674–9754.
34 G. Hazarika and P. G. Ingole, *Mater. Today Chem.*, 2024, **38**, 102109.
35 A. Kozlovskiy, D. Borgekov, I. Kenzhina, M. Zdorovets, I. Korolkov, E. Kaniukov, M. Kutuzau and A. Shumskaya, *Springer Proc. Phys.*, 2019, **221**, 461–479.
36 A. B. Yeszhanov, I. V Korolkov, A. Kh Shakayeva, L. I. Lissovskaya and M. V Zdorovets, *Eurasian J. Chem.*, 2023, **110**, 131–138.
37 A. K. Shakayeva, A. B. Yeszhanov, A. T. Zhumazhanova, I. V. Korolkov and M. V. Zdorovets, *Eurasian J. Chem.*, 2024, **29**, 81–88.
38 A. A. Mashentseva, N. Seitzhapar, M. Barsbay, N. A. Aimanova, A. N. Alimkhanova, D. A. Zheltov, A. M. Zhumabayev, B. S. Temirgaziev, A. A. Almanov and D. T. Sadyrbekov, *RSC Adv.*, 2023, **13**, 26839–26850.
39 I. B. Muslimova, D. D. Omertassov, N. Zhumanazar, N. Assan, Z. K. Zhatkanbayeva and I. V. Korolkov, *Polym.*, 2025, **17**, 2221.
40 N. Zhumanazar, A. B. Yeszhanov, G. B. Melnikova, A. T. Zhumazhanova, S. A. Chizhik and I. V Korolkov, *ChemEngineering*, 2025, **9**, 88.
41 A. A. Mashentseva, D. S. Sutekin, S. R. Rakisheva and M. Barsbay, *Polym.*, 2024, **16**, 2616.
42 M. Usman, M. Ali, B. A. Al-Maythalony, A. S. Ghanem, O. W. Saadi, M. Ali, M. A. Jafar Mazumder, S. Abdel-Azeim, M. A. Habib, Z. H. Yamani, W. Ensinger and B. A. Al-Maythalony, *ACS Appl. Mater. Interfaces*, 2020, **12**, 49992–50001.
43 F. Caddeo, R. Vogt, D. Weil, W. Sigle, M. E. Toimil-Molares and A. W. Maijenburg, *ACS Appl. Mater. Interfaces*, 2019, **11**, 25378–25387.
44 D. D. Omertassov, A. K. Shakayeva, Z. K. Zhatkanbayeva, R. I. Shakirzyanov, M. V. Zdorovets, O. Güven and I. V. Korolkov, *ACS Omega*, 2025, **10**, 30271.
45 D. W. Fox, D. X. Antony, Y. Y. L. Sip, J. Fnu, A. Rahmani, T. Jurca and L. Zhai, Electrospun hydrogel fibers guide HKUST-1 assembly, *Mater. Today Commun.*, 2022, **33**, 104535.
46 M. Ciulla, V. Canale, R. D. Wolicki, S. Pilato, P. Bruni, S. Ferrari, G. Siani, A. Fontana and P. Di Profio, *Separations*, 2023, **10**, 505.
47 Y. Zhang, Y. Zhang, X. Wang, J. Yu and B. Ding, Ultrahigh Metal–Organic Framework Loading and Flexible Nanofibrous Membranes for Efficient CO_2 Capture with Long-Term, Ultrastable Recyclability, *ACS Appl. Mater. Interfaces*, 2018, **10**(40), 34802–34810.
48 H. M. A. Hassan, M. S. Alruwaili, I. H. Alsohaimi, M. A. El-Hashemy, A. A. Alqadami, K. Alshammari, I. K. Alali,

S. J. F. Alanazi and M. R. El-Aassar, *Diam. Relat. Mater.*, 2024, **149**, 111649.
49 P. Küsgens, M. Rose, I. Senkovska, H. Fröde, A. Henschel, S. Siegle and S. Kaskel, *Microporous Mesoporous Mater.*, 2009, **120**, 325–330.
50 F. Gul-E-Noor, B. Jee, A. Pöppl, M. Hartmann, D. Himsl and M. Bertmer, *Phys. Chem. Chem. Phys.*, 2011, **13**, 7783–7788.
51 J. B. Decoste, M. S. Denny, G. W. Peterson, J. J. Mahle and S. M. Cohen, Enhanced aging properties of HKUST-1 in hydrophobic mixed-matrix membranes for ammonia adsorption, *Chem. Sci.*, 2016, **7**, 2711–2716.
52 N. Ding, H. Li, X. Feng, Q. Wang, S. Wang, L. Ma, J. Zhou and B. Wang, *J. Am. Chem. Soc.*, 2016, **138**, 10100–10103.
53 F. Brandani and D. M. Ruthven, *Ind. Eng. Chem. Res.*, 2004, **43**, 8339–8344.
54 A. Zulfi, Y. A. Rezeki, D. Edikresnha, M. M. Munir and K. Khairurrijal, Synthesis of Fibers and Particles from Polyvinyl Chloride (PVC) Waste Using Electrospinning, *IOP Conf. Ser. Mater. Sci. Eng.*, 2018, **367**, 012014.
55 A. U. Razzaq, D. J. McEachern, P. A. Rupar, P. R. Willis, S. N. Mahmoodi and M. R. Esfahani, *ACS Appl. Eng. Mater.*, 2023, **1**, 1924–1936.
56 R. Amalia, A. Noviyanto, L. A. Rahma, Merita, A. Labanni, M. Fahroji, S. Purwajanti, D. A. Hapidin and A. Zulfi, PVC waste-derived nanofiber: Simple fabrication with high potential performance for PM removal in air filtration, *Sustain. Mater. Technol.*, 2024, **40**, e00928.
57 M. A. Keane, *ChemSusChem*, 2009, **2**, 207–214.
58 G. Sneddon, J. C. Mcglynn, M. S. Neumann, H. M. Aydin, H. H. P. Yiu and A. Y. Ganin, *J. Mater. Chem. A*, 2017, **5**, 11864–11872.
59 M. S. Samuel, K. V. Savunthari and S. Ethiraj, *Environ. Sci. Pollut. Res.*, 2021, **28**, 40835–40843.
60 P. Iacomi, U-Hwang Lee, Anil H. Valekar, Jong-San Chang and Philip L. Llewellyn, Investigating the effect of alumina shaping on the sorption properties of promising metal–organic frameworks, *RSC Adv.*, 2019, **9**, 7128–7135.
61 L. L. Jiang, X. Zeng, M. Li, M. Q. Wang, T. Y. Su, X. C. Tian and J. Tang, *RSC Adv.*, 2017, **7**, 9316–9320.
62 A. S. Abou-Elyazed, A. I. Ftooh, Y. Sun, A. G. Ashry, A. K. F. Shaban, A. M. El-Nahas and A. M. Yousif, *ACS Omega*, 2024, **9**, 37662–37671.
63 G. Camarillo-Martínez, E. Martínez-Cano, A. Zepeda-Navarro, J. L. Guzmán-Mar and E. Y. Bivián-Castro, *Int. J. Mol. Sci.*, 2025, **26**, 5777.
64 L. Sondermann, Q. Smith, T. Strothmann, A. Vollrath, T. Hai, Y. Beglau and C. Janiak, *RSC Mechanochemistry*, 2024, **1**, 296–307.
65 S. Roy, J. Darabdhara and M. Ahmaruzzaman, *RSC Sustain.*, 2023, **1**, 1952–1961.
66 S. S. Y. Chui, S. M. F. Lo, J. P. H. Charmant, A. G. Orpen and I. D. Williams, *Science*, 1999, **283**, 1148–1151.
67 N. Sahiner, K. Sel, O. Faruk, S. Demirci and G. Terzi, *Appl. Surf. Sci.*, 2014, **314**, 663–669.
68 B. H. Bowser, L. J. Brower, M. L. Ohnsorg, L. K. Gentry, C. K. Beaudoin and M. E. Anderson, Comparison of Surface-Bound and Free-Standing Variations of HKUST-1 MOFs: Effect of Activation and Ammonia Exposure on Morphology, Crystallinity, and Composition, *Nanomaterials*, 2018, **8**(9), 650.
69 A. Yañez-Aulestia, V. M. Trejos, J. M. Esparza-Schulz, I. A. Ibarra and E. Sánchez-González, Chemically Modified HKUST-1(Cu) for Gas Adsorption and Separation: Mixed-Metal and Hierarchical Porosity, *ACS Appl. Mater. Interfaces*, 2024, **16**(47), 65581–65591.
70 N. Vrtovec, M. Mazaj, G. Buscarino, A. Terracina, S. Agnello, I. Arčon, J. Kovač and N. Zabukovec Logar, *Cryst. Growth Des.*, 2020, **20**, 5455–5465.
71 N. Al-Janabi, P. Hill, L. Torrente-Murciano, A. Garforth, P. Gorgojo, F. Siperstein and X. Fan, *Chem. Eng. J.*, 2015, **281**, 669–677.
72 W. Wong-Ng, J. A. Kaduk, D. L. Siderius, A. L. Allen, L. Espinal, B. M. Boyerinas, I. Levin, M. R. Suchomel, J. Ilavsky, L. Li, I. Williamson, E. Cockayne and H. Wu, *Powder Diffr.*, 2015, **30**, 2–13.
73 Y. Liu, P. Ghimire and M. Jaroniec, *J. Colloid Interface Sci.*, 2019, **535**, 122–132.
74 K. L. Andrea Domána, János Madarászb, *Thermochim. Acta*, 2017, **647**, 62–69.
75 A. B. Yeszhanov, A. K. Shakayeva, M. V. Zdorovets, D. B. Borgekov, A. L. Kozlovskiy, P. V. Kharkin, D. A. Zheltov, M. V. Krasnopyorova, O. Güven and I. V. Korolkov, Hybrid Membranes Based on Track-Etched Membranes and Nanofiber Layer for Water–Oil Separation and Membrane Distillation of Low-Level Liquid Radioactive Wastes and Salt Solutions, *Membranes*, 2025, **15**(7), 202.
76 P. Jia, R. Wang, L. Hu, M. Zhang and Y. Zhou, *Polish J. Chem. Technol.*, 2017, **19**, 16–19.
77 L. Qiu, L. Wang, M. Zhang, M. Zhang, M. Wang, C. Yang, R. Li and G. Wu, *Microporous Mesoporous Mater.*, 2020, **292**, 109723.
78 A. Pal, S. Chand, S. M. Elahi and M. C. Das, *Dalt. Trans.*, 2017, **46**, 15280–15286.
79 R. Walczak, A. Savateev, J. Heske, N. V. Tarakina, S. Sahoo, J. D. Epping, T. D. Kühne, B. Kurpil, M. Antonietti and M. Oschatz, *Sustain. Energy Fuels*, 2019, **3**, 2819–2827.
80 M. R. Ryder, B. Civalleri, G. Cinque and J. C. Tan, *CrystEngComm*, 2016, **18**, 4303–4312.
81 J. Yu, L. Sun, C. Ma, Y. Qiao and H. Yao, *Waste Manag.*, 2016, **48**, 300–314.
82 Z. Liang, M. Marshall and A. L. Chaffee, *Energy and Fuels*, 2009, **23**, 2785–2789.
83 C. Zhou, L. Cao, S. Wei, Q. Zhang and L. Chen, *Comput. Theor. Chem.*, 2011, **976**, 153–160.
84 R. Poloni, B. Smit and J. B. Neaton, *J. Phys. Chem. A*, 2012, **116**, 4957–4964.
85 C. Choi, R. L. Kadam, S. Gaikwad, K. Hwang and S. Han, *Microporous Mesoporous Mater.*, 2020, **296**, 110006.
86 R. Girimonte, D. Sofia, S. Agrippino, M. Turano and F. Testa, *Chem. Eng. Trans.*, 2024, **111**, 577–582.
87 Z. Fateminia, H. Chiniforoshan and V. Ghafarinia, *ACS Omega*, 2023, **8**, 22742–22751.

88 J. Sun, M. Shang, M. Zhang, S. Yu, Z. Yuan, X. Yi, S. Filatov and J. Zhang, *Carbohydr. Polym.*, 2022, **293**, 119720.
89 H. Zhao, N. Zhao, Q. Wang, F. Li, F. Wang, S. Fan, E. V. Matus, Z. R. Ismagilov, L. Li and F. Xiao, *J. CO_2 Util.*, 2021, **44**, 101415.
90 F. Raganati, M. Alfe, V. Gargiulo, R. Chirone and P. Ammendola, *Chem. Eng. J.*, 2019, **372**, 526–535.
91 C. Goel, H. Kaur, H. Bhunia and P. K. Bajpai, *J. CO_2 Util.*, 2016, **16**, 50–63.